Correspondence to:
S. Zhang,
shzhang@uw.edu

Instabilities in nonlinear internal waves on the Washington continental shelf

Shuang Zhang[1,2] and Matthew H. Alford[2,3]

[1]Applied Physics Laboratory, University of Washington, Seattle, Washington, USA, [2]School of Oceanography, University of Washington, Seattle, Washington, USA, [3]Scripps Institution of Oceanography, University of California San Diego, La Jolla, California, USA

Abstract Previous studies have identified two primary mechanisms (shear instability and convective instability) by which nonlinear internal waves (NLIWs) induce mixing on continental shelves. To determine the relative importance of these and their dependence on background flow conditions, we examine a much longer (6 month) data set from a moored ADCP/thermistor chain with 2 m vertical spacing in which over 600 NLIWs are detected. Turbulent properties of the 318 waves with detectable overturning instabilities are documented using Thorpe scales. The 130 waves detected while an ADCP was functioning are classified based on a Froude number criterion ($Fr = \frac{u}{c}$, where u is velocity in the wave propagation direction, c is the wave phase speed). Of these, 108 waves are identified as shear-instability (Type I; $Fr < 1$) waves and 22 as convective instability (Type II; $Fr > 1$). Composites are constructed by averaging in a wave coordinate frame over all waves in each category, showing the mean spatial structure of dissipation and other wave quantities. Turbulence is highest at the sheared interface for Type I waves and throughout the wave core for Type II waves. No relationship between wave instability mechanisms and wave/background parameters such as wave steepness, stratification, or mean flow is found, except that unstable waves tend to be more energetic, demonstrating a need to better understand wave propagation and breaking in complex and variable coastal oceanographic background flows.

1. Introduction

Nonlinear internal waves (NLIWs) are commonly observed on continental shelves around the globe. Observations of strong turbulence within NLIWs have been reported [e.g., *Sandstrom and Oakey*, 1995; *Stanton and Ostrovsky*, 1998; *Duda and Farmer*, 1999; *Moum et al.*, 2003; *MacKinnon and Gregg*, 2003], identifying them as an important mechanism for mixing in coastal regions [e.g., *Moum et al.*, 2007a, 2007b; *D'Asaro et al.*, 2007]. NLIWs create conditions favorable for instabilities and can give rise to half of the midwater-column dissipation on continental shelves [e.g., *MacKinnon and Gregg*, 2003]. This indicates that NLIW energy is not simply deposited in the surf zone but rather that a considerable portion is lost as waves propagate over the shelf [*Moum et al.*, 2003, 2007a]. Accordingly, patterns of nutrients and other quantities will depend on the strength and time/space dependence of NLIW mixing. Mixing associated with internal waves has been tied to enhanced vertical nutrient fluxes, in some cases controlling local productivity, e.g., the New Zealand shelf [*Sharples et al.*, 2009], the Scotian shelf [*Sandstrom and Elliott*, 1984], and off the coast of Mauritania [*Schafstall et al.*, 2010]. Breaking internal waves at Dongsha Atoll in the SCS have a possible role of the microbial food web on nutrient regeneration in a tropical reef ecosystem [*Wang et al.*, 2007]. Thus, understanding the strength, mechanisms, and parameter dependence of NLIW mixing is an important area of coastal research.

Lamb [2014] described four primary instability mechanisms through which NLIWs can give rise to mixing: (1) shear instabilities triggered by NLIW-induced vertically sheared currents, (2) convectively unstable wave cores, (3) instabilities in the bottom boundary layer, and (4) wave breaking during sudden shoaling at abrupt topography. The former two mechanisms (Figure 1) are dominant for midcolumn mixing apart from rapid bathymetric changes, and are consistent with the observations in *Moum et al.* [2003] and *Shroyer et al.* [2010], who categorized them as Type I and Type II waves, respectively. While pioneering, one shortcoming of these previous studies was their inclusion of a small number of waves. Hence, the generality of the results and their dependence on wave properties such as velocity, shear, and wave amplitude displacement are unknown.
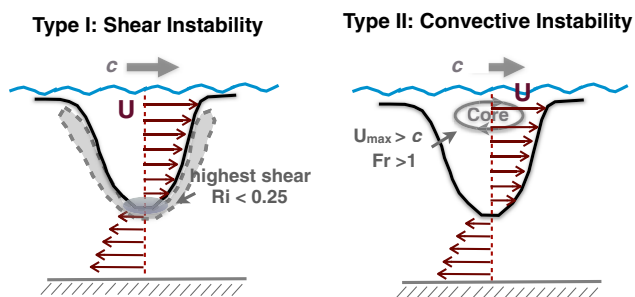
Figure 1. A cartoon showing wave breaking by shear instability (Type I) and convective instability in the wave core (Type II).

In this study, we take advantage of a 6 month moored time series on the Washington continental shelf (Figure 2) in which 318 waves with overturning instabilities (out of a total of 657 waves) are measured at high vertical and temporal resolution. We use a Froude number criterion ($Fr = \frac{u}{c}$) [*Gill*, 1982] to classify the detected waves into shear-instability (Type I; $Fr < 1$) waves and convective-instability (Type II; $Fr > 1$) waves (Type I waves would be better identified using a Richardson number criterion *Miles* [1961]

and *Howard* [1961], but our shear is not sufficiently resolved for this analysis, as explained below). Properties of these two types of waves are similar to those identified by *Lamb* [2014] and *Shroyer et al.* [2010]: (I) elevated dissipation concentrated at the waves' sheared interface (white contours in wave #1 in Figure 3), and (II) elevated dissipation distributed throughout the wave core (wave #2 in Figure 3). The large number of waves allows us to form composites in a wave coordinate frame to examine the spatial structure of the mixing associated with each mechanism, and to statistically examine their relative importance. This study expands previous studies of *Moum et al.* [2003] and *Shroyer et al.* [2010] by (1) documenting NLIW-induced instabilities and their temporal variation; (2) categorizing waves based on instability mechanisms (shear instability and convective instability/unstable cores); and (3) exploring general patterns of NLIW-induced mixing based on a longer time series.

A major shortcoming of our moored data set is the lack of direct microstructure measurements. Instead, we employ the method of Thorpe scales [*Thorpe*, 1977], which measures the outer scale L_T of turbulence by resorting statically unstable profiles, whence the dissipation rate ϵ can be estimated [e.g., *Dillon*, 1982]. Though the 2 m vertical spacing between sensors is relatively coarse for this purpose, wave turbulence is sufficiently intense that overturns are nonetheless detectable in many waves. Though the smallest turbulence patches are not detected, the largest events generally dominate the mean value [*Levine and Boyd*, 2006; *M. H. Alford and Pinkel*, 2000]. We consider these effects in our analysis.
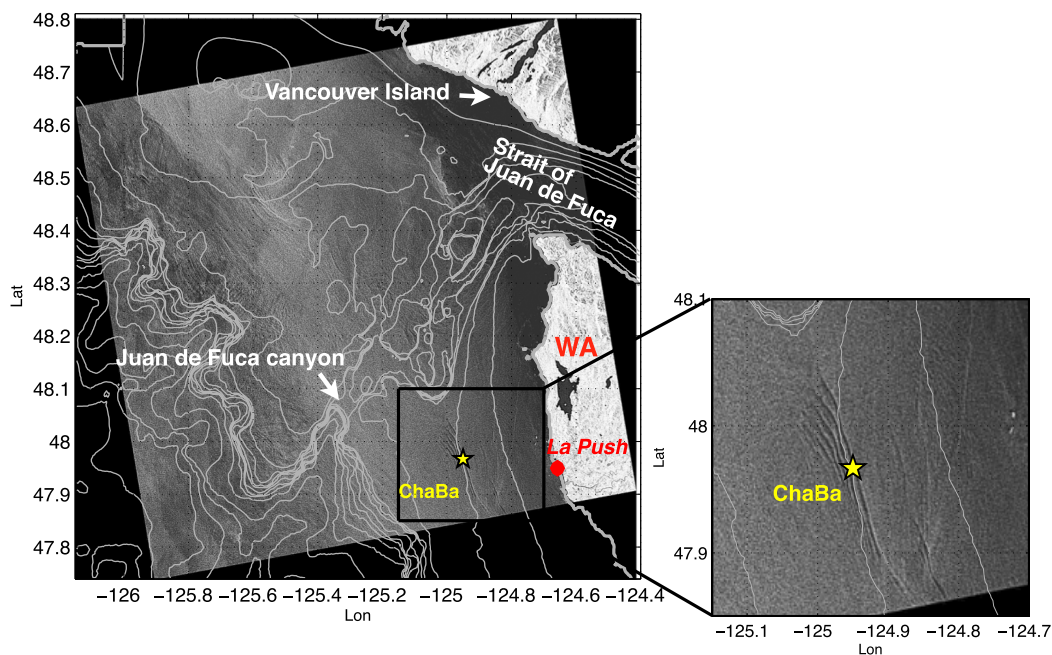

Figure 2. A SAR image captured by Radarsat-2 on 16 July 2011, 02:09:21 UTC with bathymetry superimposed. Inset shows a nonlinear internal wave train passing by the *ChaBa* mooring (yellow star).
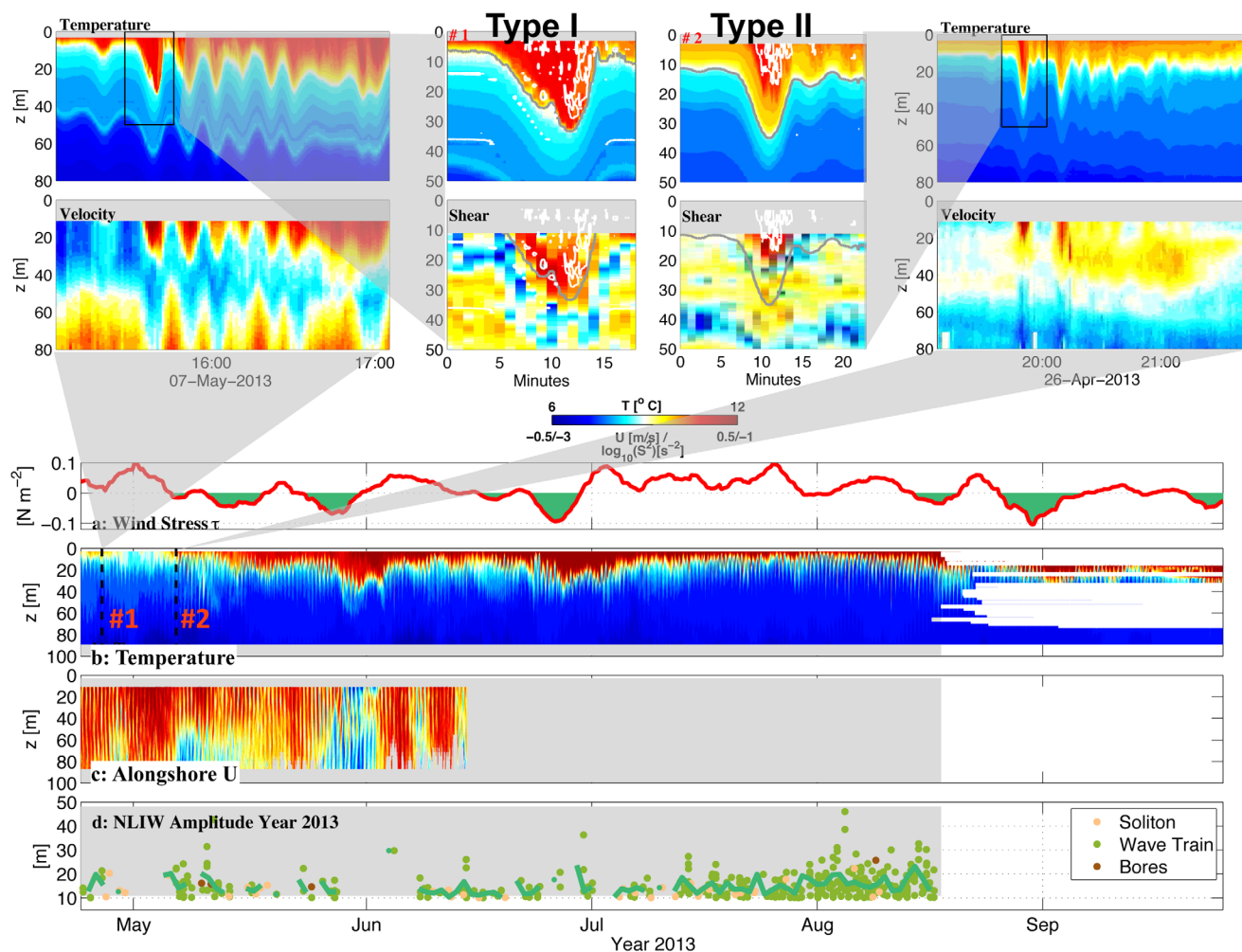
Figure 3. (a) Time series of the mooring data and nonlinear internal wave examples, showing alongshore wind stress (southeastward as positive; northwestward (upwelling favorable) are shaded in green); (b) temperature; (c) alongshore velocity (southeastward as positive); and (d) NLIW amplitude, colored by wave shape (see text), and their running 1 day mean. Black dashed lines in Figure 3b indicate arrivals of two wave examples #1 and #2 (subplots) for Type I and Type II waves (see text), respectively. Waves in subplots are given by time series of temperature, velocity, and 4 m vertical shear. Gray and green contours indicate the 9°C isotherm and temperature inversions, respectively.

This paper is organized as follows. The experiment, data, and techniques are presented in section 2. Background oceanographic background and basic characteristics of the observed NLIWs are described in section 3. Wave categorization based on instability mechanisms is documented in section 4. Wave composites in each category are described in section 5, followed by a summary and discussion in section 6.

2. Experimental Details

2.1. Data

Data used in this study are from the "*ChaBa*" surface mooring, designed and maintained by University of Washington as part of the Northwest Association of Networked Ocean Observing Systems (NANOOS). *ChaBa* (47°58.0′N, 124°57.0′W) was deployed for five successive summers/falls from 2010 to 2014 in 100 m deep water ~25 km off La Push, WA (Figure 2). The mooring site is relatively flat (slope < 0.01) and about 30 km away from the shelf break. NLIWs in the first 3 years were reported in *Zhang et al.* [2015]. Data used in this study are from the deployment during 24 April 2013 to 23 September 2013, which augmented the temperature and salinity measurements from conductivity-temperature-depth (CTD) sensors in the previous years with much more highly vertically resolved temperature measurements and faster velocity sampling. Temperature was measured every 3 s by 40 Seabird Electronics (SBE) 56 T-loggers spaced over a 2 m interval between the surface and 80 m depth (Figure 3b). A downward-looking 300 kHz Workhorse ADCP at 3 m
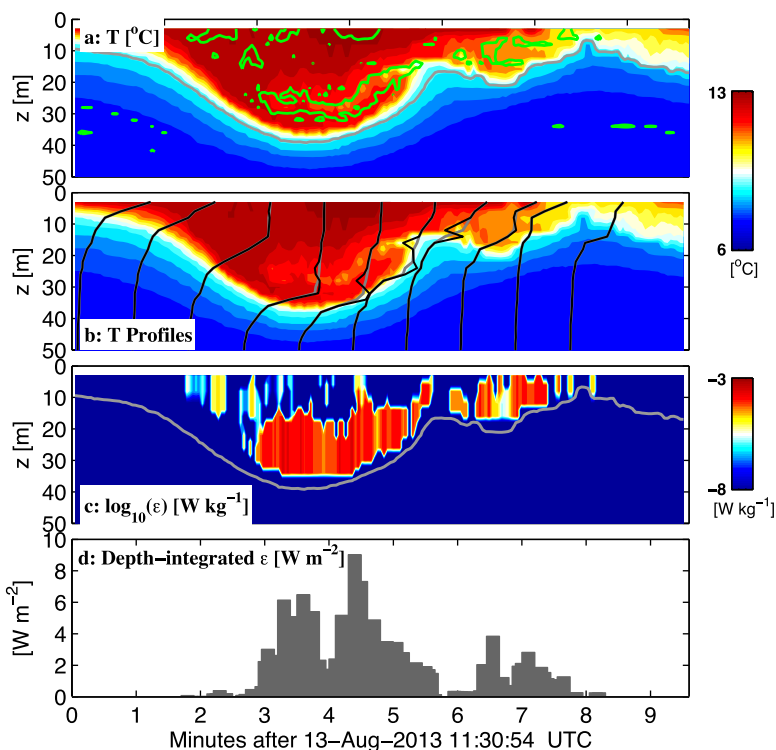
Figure 4. A wave example with large temperature overturns detected on 13 August 2013, showing (a) temperature (green and gray contours show temperature inversions and the 9°C isotherm, respectively); (b) temperature profiles (black) every 30 s and their sorted profiles (gray dashed); (c) dissipation rate estimated from Thorpe scales (gray contours the 9°C isotherm); and (d) depth-integrated dissipation rate.

depth recorded near-full-depth velocity profiles every 1 min at a 4 m interval from 24 April to 14 June until the batteries were depleted (Figure 3c). Wind measurements (Figure 3a) are from National Data Buoy Center (NDBC) Station DESW1 at Destruction Island, located at 47°40.5′N, 124°29.1′W, about 30 km away from *ChaBa* to the east.

2.2. Calculation of Dissipation Rate Using Thorpe Scale

We do not measure turbulence directly in this experiment, and surface wave pumping precludes calculation of dissipation rate using the Bachelor wave number method [*M. Alford and Pinkel*, 2000; *Moum and Nash*, 2009]. We instead estimate dissipation rate using overturning (Thorpe) scales L_T computed from the vertically discrete thermistors following *Levine and Boyd* [2006]. Dissipation rate ϵ is given by $\epsilon = 0.64 L_T^2 N^3$ [*Dillon*, 1982], where N is the buoyancy frequency computed from sorted density profiles. The method has been demonstrated in multiple experiments [e.g., *MacKinnon and Gregg*, 2005; *Alford et al.*, 2006] to give values of ϵ within a factor of two of direct measurements. Recent modeling work by *Mater et al.* [2013] gives rise to the possibility that epsilon from overturns may be biased high as much as 2–6 in some regions. These effects are still being explored, but in any case do not affect our results which focus on the spatial structure rather than the magnitude of turbulence.

Though 4 times finer than that of *Levine and Boyd* [2006], our sensor spacing of 2 m is still relatively coarse given the strong coastal stratification at our site. The minimum detectable overturn of 2 m corresponds to a Thorpe displacements L_T^{min} of ∼1 m, giving a sensitivity in dissipation rate of $\epsilon^{min} \sim O(10^{-6})\,\mathrm{W\,kg^{-1}}$, depending on N—far too coarse to detect open-ocean turbulence. However, sufficient waves at our site have such strong turbulence that our coarse resolution does not materially affect our analysis. An example NLIW with well-resolved turbulence displays temperature overturns up to 15 m (Figure 4). In this example, temperature profiles (Figure 4a) plunge nearly 25 m at the wave's leading edge in several minutes. Before the maximum displacement, turbulent overturns ∼5 m appear near the interface (Figure 4b), corresponding to a dissipation rate of $O(10^{-5}) - O(10^{-4})\,\mathrm{W\,kg^{-1}}$ (Figure 4c). Immediately after, overturns develop to 15 m and the interface then becomes actively turbulent throughout the trailing edge and the wave's wake.
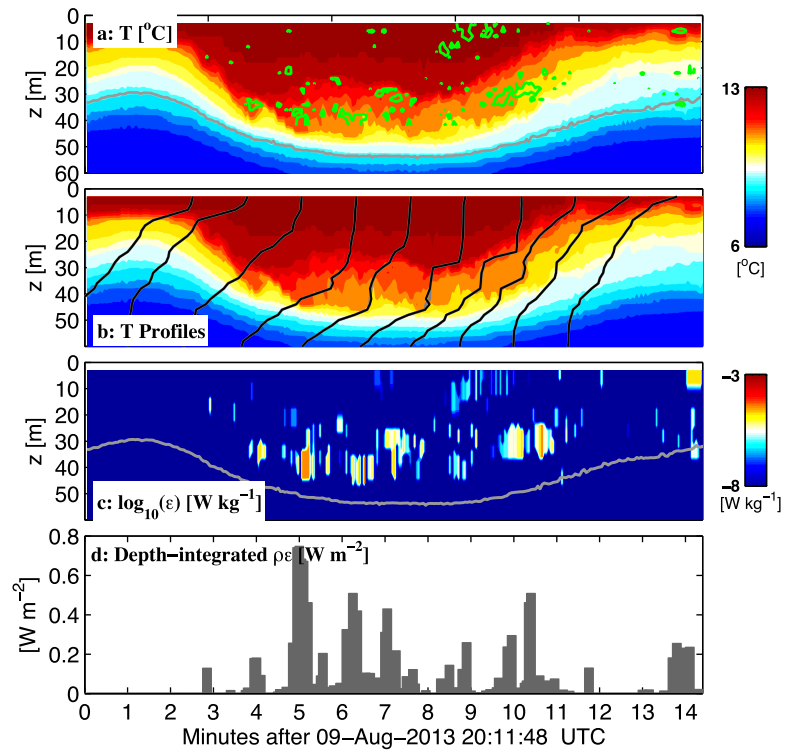
Figure 5. Same as Figure 4 but for a wave with small temperature overturns detected on 9 August 2013.

Depth-integrated dissipation (Figure 4d) has a maximum value $\sim 9\,\mathrm{W\,m^{-2}}$ immediately following the maximum displacement, with secondary peaks just before the wave trough and in the turbulent wake. As an example of mixing events that are nearer to our detection threshold, a series of small overturns (2–5 m) are recorded along the interface of a wave on 9 August 2013 (Figure 5); the corresponding dissipation rate is estimated to be $\epsilon \sim O(10^{-6})\,\mathrm{W\,kg^{-1}}$ near the interface.

Persistent lateral thermohaline intrusions exist at our site, usually below the thermocline (e.g., Figures 6 and 7, white). Since they are statically stable, these would introduce large overestimates in the temperature-
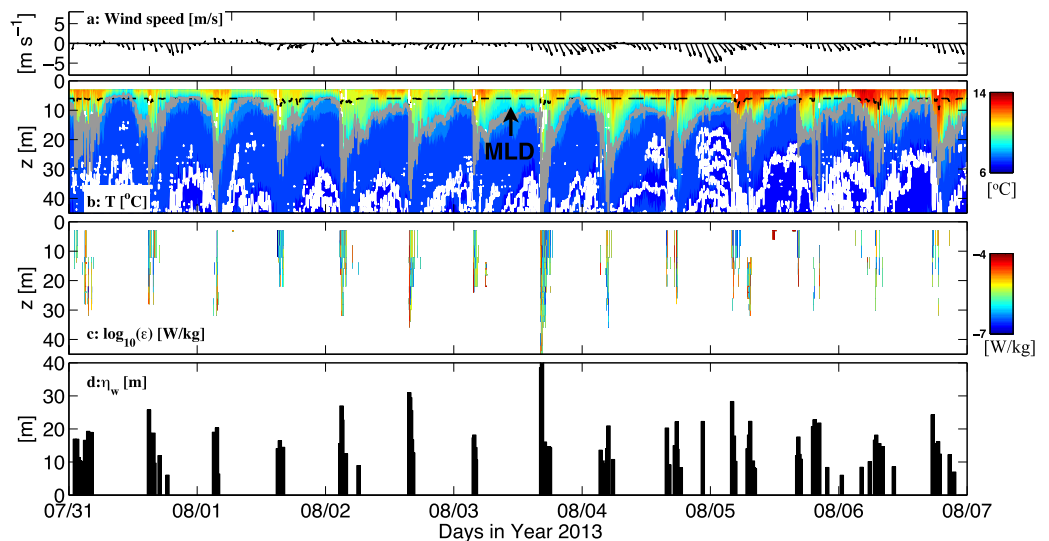

Figure 6. A 7 day period showing a scenario of weak winds and strong waves during 7–14 August 2013, with time series of (a) wind speed, (b) temperature, (c) dissipation rate, and (d) NLIW amplitude. The black dashed line and gray lines in Figure 6b indicate mixed-layer depth (MLD) and the 9°C isotherm, respectively. Temperature inversions are contoured in white. Below the 9°C isotherm, these are dominated by statically stable thermohaline intrusions rather than density overturns.
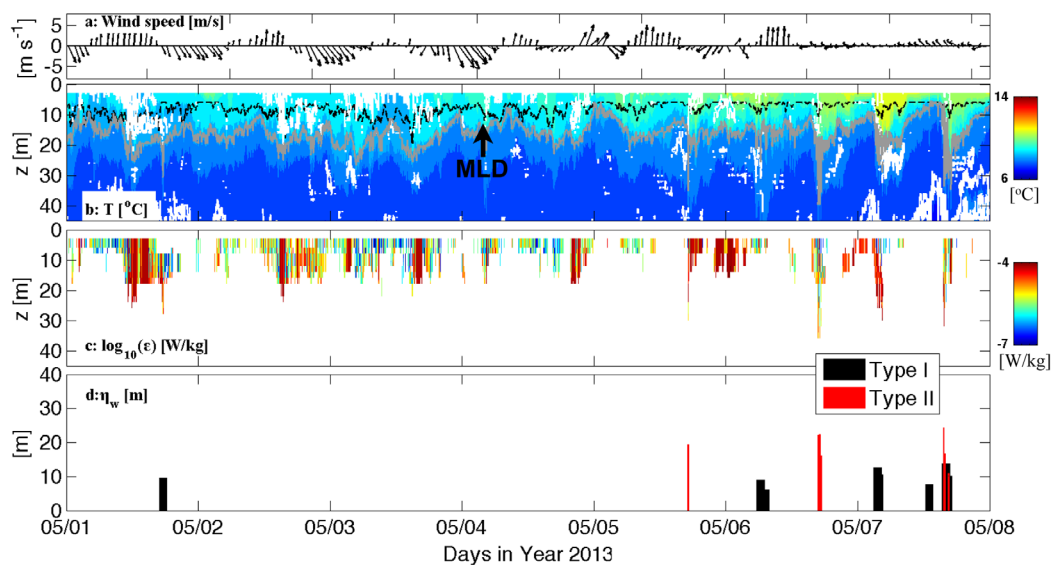
Figure 7. A 7 day period showing a scenario of weak winds and strong waves during 1–8 May 2013, with time series of (a) wind speed, (b) temperature, (c) dissipation rate, and (d) NLIW amplitude, colored by wave category (Type I as black and Type II as red). The black dashed line and gray line in Figure 7b indicate mixed-layer depth (MLD) and the 8.5°C isotherm, respectively.

based Thorpe scale calculation if not properly screened. Therefore, we focus on mixing within the thermocline above a certain isotherm depth, which is a value between 8°C and 9°C to exclude deep intrusions during the period. Also, intrusions generally have much a longer duration (hours) than NLIWs (~10–15 min). Thus, they are easily distinguished by comparing the time scale of overturning events to that of the waves.

3. Oceanographic Background and Basic Characteristics of NLIW

The Washington's continental shelf has a seasonal wind-driven circulation. In summer/early fall, northwesterly winds are predominant (Figure 3a), generating a cross-shelf density gradient that sustains a southeastward shelf current (Figure 3c). The observed stratification is strong and concentrated near the surface (Figure 3b). In fall, winds are stronger and southerly bursts more common (Figure 3a, green shading). The stratification is weaker and the pycnocline deeper (Figure 3b).

Six hundred and fifty-seven NLIWs are detected in our 2013 records, of which almost all are internal solitary waves arriving in wave trains at semidiurnal intervals, with only a few bores (Figure 3d). In general, NLIW characteristics in 2013 are similar to the previous 3 years, which are described in detail in *Zhang et al.* [2015]. Because NLIW energy flux is in the same direction (onshore; toward the northeast) and correlated in magnitude with that of the internal tide, *Zhang et al.* [2015] concluded that the NLIW are generated by shoaling of a remotely incident internal tide. A striking aspect of the NLIW is that though they nearly all appear to be mode-1 waves of depression, they show a variety of morphologies, including internal solitary waves, solitary wave trains, and bores. These characteristics do not appear related to background conditions such as stratification or low-frequency currents at the mooring, whose strong variability can be seen in the 2013 records reported here (Figure 3). This suggests a strong sensitivity of the generation process and the waves' subsequent propagation to conditions at the shelf break. The dependence of the wave morphology on background conditions is expected given previous theoretical and modeling studies [e.g., *Lamb*, 2014]; notably, the background currents are comparable to the wave speeds (~0.4 m s^{-1}), and their strong and variable shear can strongly modulate the waves (e.g., via the Taylor-Goldstein equation).

These variable background conditions have a profound but complicated impact on the NLIWs and their mixing, as demonstrated by 2 week long examples (Figures 6 and 7). During summer/early fall, strong, regular NLIWs are abundant throughout the records (Figure 3d). Winds are weak (Figure 6a). A total of 97 NLIWs are detected in this period (Figures 6b and 6d), all of which are mode-1 depression waves. NLIWs generally arrive semidiurnally in wave trains at internal tide depressions, with a mean (max) wave amplitude of 18 m (36 m). Stratification is strong during this period, with a stable, shallow mixed-layer depth (that where

temperature is 0.2°C absolute difference from surface) of ∼5–8 m. Enhanced dissipation rates ($\sim O(10^{-6})$ W kg^{-1}) occur twice a day in the thermocline, closely following the arrivals of nonlinear internal wave trains during this period (Figures 6c and 6d).

During spring, fewer and smaller NLIWs are detected (Figure 3), whose arrivals are irregular. A 7 day period during 1–8 May 2013 shows strong and oscillating winds, with a mean speed of 3.4 m s^{-1} (Figure 7a). During most of the record, the near-surface water is sufficiently mixed by winds, decreasing the stratification in the upper water column and bringing down the mixed-layer depth to ∼12–17 m. Only 15 NLIWs are detected in this period, with a mean (max) wave amplitude of 14 m (24 m) (Figures 7b and 7d), much smaller than those detected in Figure 6, presumably due to the weak stratification and lack of a strong pycnocline to serve as a waveguide [*Zhang et al.*, 2015]. Dissipation in the thermocline ($\sim O(10^{-5})$ W kg^{-1}) is not visually associated with arrivals of NLIWs. More regular NLIWs appear on 6 May, which are more correlated with the elevated dissipation rates during 7 and 8 May.

4. Categorization of NLIWs Based on Instability Mechanisms

Of the 657 waves observed, 318 (48.4%) show detectable overturning events; the corresponding dissipation rates are calculated following the method described in section 2.2. The spatial structure of the turbulence is variable, but can be loosely grouped into shear-instability (Type I) waves and convective-instability (Type II) waves. In agreement with *Lamb* [2014] and *Shroyer et al.* [2010], most Type I waves have high dissipation confined to the waves' sheared interface, presumably due to shear instabilities triggered by NLIW-induced vertically sheared currents. On the other hand, Type II waves usually have elevated dissipation distributed throughout the wave core, likely due to convective instability inside the core. Note that the Type II waves discussed here are distinct from waves with trapped cores [*Lamb*, 2002]. Instead, convective instability is a breaking mechanism for NLIWs, which may cause various types of breaking [e.g., wave collapsing, plunging, surging; see *Aghsaee et al.*, 2010]. An example of a Type I wave (Figure 8, left), displays overturns with enhanced dissipation starting around the wave trough, consistent with the region of highest shear and low Richardson numbers (∼0.25) at the wave interface. On the other hand, an example of Type II wave (Figure 8, right) shows high turbulence levels near the surface, colocated with the largest velocity.

We attempt to categorize the 318 NLIWs exhibiting overturns based on a dimensionless number computed for each wave. It is generally accepted that Richardson number $Ri < 0.25$ ($Ri = \frac{N^2}{S^2}$, where stratification $N^2 = -\frac{g}{\rho}\frac{d\rho}{dz}$, ρ is the potential density, and shear $S^2 = \left(\frac{\partial u}{\partial z}\right)^2$) indicates the potential for shear instabilities (Type I) [*Miles*, 1961; *Howard*, 1961], and Froude number $Fr > 1$ ($Fr = \frac{U_{max}}{c}$, where c is the Dubreil-Jacotin-Long (DJL) phase speed [*Stastna and Lamb*, 2002] and U_{max} is the maximum velocity in the wave propagation direction) indicates the potential for convective instabilities (Type II) [*Gill*, 1982; *Lamb*, 2014]. Therefore, classification could in principle be done by identifying waves with $Ri < 0.25$ as Type I and waves with $Fr > 1$ as Type II. However, because our shear records are underresolved (4 m bins), our computed Ri is not always a skillful predictor of the onset of shear instability. We therefore instead use Froude number Fr for wave characterization, i.e., $Fr < 1$ for nonconvective instabilities (Type I) and $Fr > 1$ for convective instabilities (Type II). Examples of a Type I (Figure 8, left) and Type II wave (Figure 8, right) have $Fr = 0.9$ and 1.3, respectively, consistent with this categorization.

Only the waves occurring before the ADCP failed (Figure 3 and section 2.1) can be classified, as velocity measurements are required. Of the 130 waves with overturns detected during 24 April to 14 June, 108 waves are classified as Type I waves and 22 as Type II waves, consistent with the finding of *Shroyer et al.* [2010], that most waves with highest dissipation are shear driven and focused at the trailing edge.

We next wish to explore the relationship between wave instability and (1) wave properties and (2) background conditions. For this purpose, we generate four subset wave populations: all (657 waves), nonbreaking (339), Type I (108), and Type II (22) waves, and compare the distribution of wave and background quantities between populations. Figure 9 shows the probability density functions (PDFs) of wave amplitude η_w, steepness ka, propagation direction θ_w and wave energy E_w for each population with medians and percentiles (25%–75%, 9%–91%) for selected wave properties indicated with "bars and whiskers." Wave steepness here is calculated as $ka = 2\pi/\lambda_w \cdot \eta_w$, where λ_w, η_w are wavelength and amplitude, respectively. E_w is total wave energy integrated over depth and wave duration. Details of the calculation of each wave property are discussed in *Zhang et al.* [2015]. No significant differences between the wave subsets are noted, except that Type II waves tend to have somewhat greater amplitude, steepness, and energy than Type I or
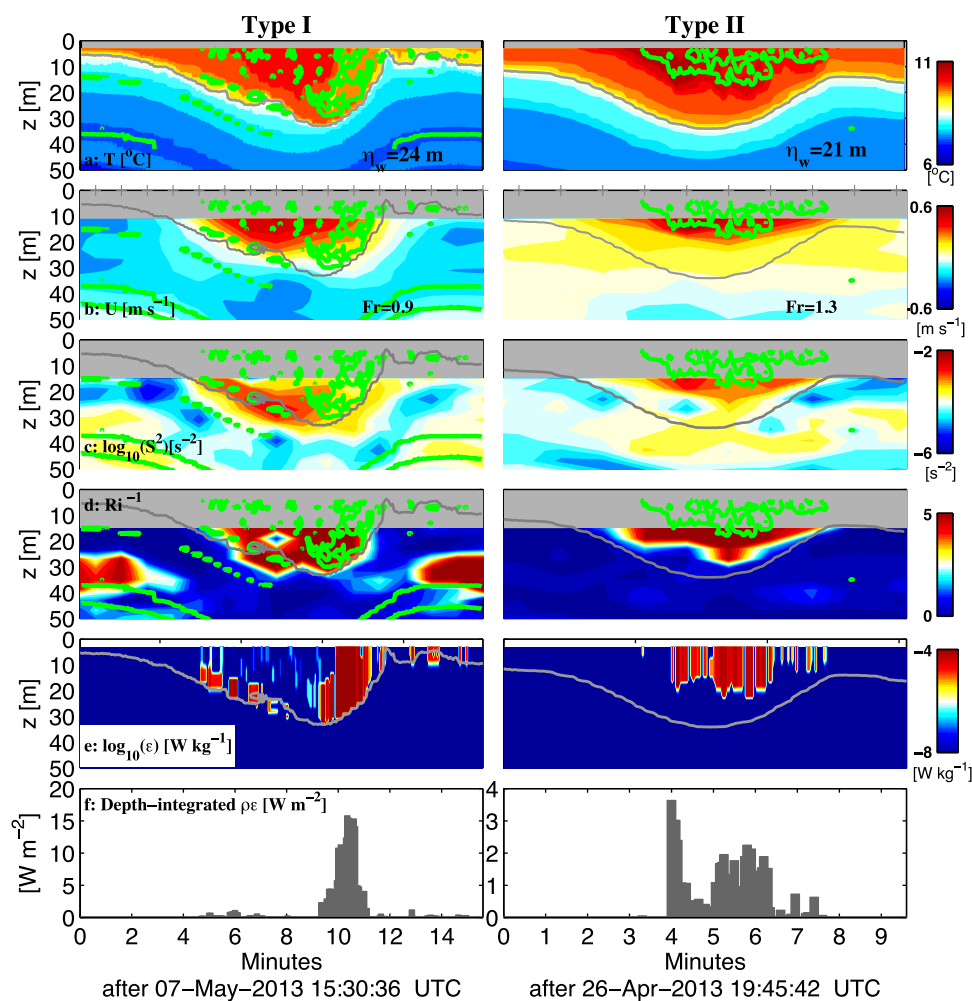
Figure 8. Examples of a (left) Type I and a (right) Type II wave, showing time series of (a) temperature, (b) velocity in the wave propagation direction, (c) 4 m shear $log_{10}(S^2)$, (d) inverse Richardson number Ri^{-1}, (e) dissipation rate $log_{10}(\epsilon)$, and (f) depth-integrated dissipation. Green contours in Figures 8a–8d indicate temperature inversions.

nonoverturning waves; Type I are marginally elevated in each of these quantities over nonoverturning waves. Type II waves also appear to be traveling slightly more toward the north.

The corresponding analysis for background parameters (Figure 10) compares the PDFs for the background near-surface stratification $log_{10}N_0^2$, mixed-layer depth (MLD), background flow U_0 and shear $log_{10}S_0^2$ in the wave propagation direction. Here the background state is defined as the average of 5–10 min before wave arrives [*Zhang et al.*, 2015]. N_0^2 is the average background stratification in the upper 20 m. U_0 and S_0^2 are the mean of the background flow and the maximum shear over depth, respectively. Type I and Type II waves tend to have somewhat weaker N_0^2 compared to the rest of waves (Figure 10a). Otherwise, background conditions appear to have no effect on either overturning occurrence or mechanism. This is also demonstrated in Figure 7 where the occurrence of each wave type appears to be random. The possible reasons for the lack of correlation between wave-induced mixing and background parameters are discussed in section 6.

5. Wave Composites

5.1. Calculation and Composites Over All Waves

The average spatial structure of wave quantities (e.g., dissipation rate, shear, velocity) is examined by taking the composite or average, over all waves in category, of the depth/time structure of each quantity. The method takes advantage of the similarity in the shape of most waves ("$sech^2$-like") to conduct the average
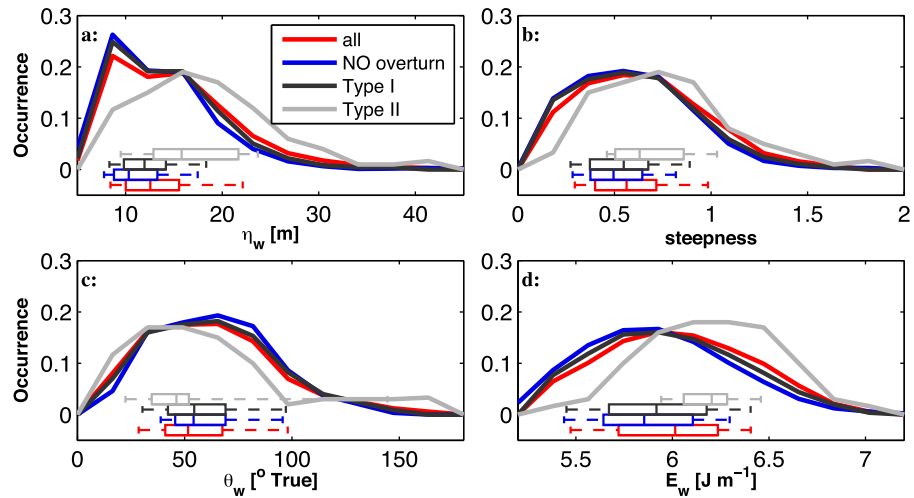
Figure 9. Probability density function (PDF) plots of (a) wave amplitude η_w, (b) steepness ka, (c) propagation direction θ_w, and (d) total wave energy for four wave populations: all waves (red, number of waves: 657), waves without overturns (blue, 339), Type I wave (black, 108), and Type II wave (light gray, 22). Box plots with whiskers show the medians and percentiles (25%–75%, 9%–91%) for each wave population.

in wave coordinates. (Bores are a notable exception but only a few bores are detected in the record; Figure 3d; these are excluded from this analysis.) The composite wave is generated by first computing the maximum displacement or wave amplitude η_w and horizontal wavelength λ_w of each wave, where $\lambda_w = c_{DJL} \cdot \tau$, and τ is the wave duration. Then, all waves are averaged together in the normalized coordinates along the wave propagation direction $(\tilde{X}, \tilde{H})$ shown in Figure 11 (first row), where $\tilde{X} = (X - X(\eta_w))/\lambda_w$, $X, X(\eta_w)$ are the horizontal distance in the wave propagation direction and at the maximum wave displacement, respectively, and $\tilde{H} = H/\eta_w$, where H is the vertical displacement. The composite wave quantities, including the composite velocity $\tilde{U}$, 4 m vertical shear $\tilde{S}^2$, Richardson number $\tilde{Ri}$, dissipation rate $\tilde{\epsilon}$ and depth-integrated dissipation $\tilde{D}$, are calculated by averaging the values in the normalized wave coordinates over a particular wave set, i.e., Type I, Type II, or all the waves (Figure 11, second to fifth rows).

Of all the 318 waves with detectable overturning events (Figure 11, left column), the composite wave displacement $\tilde{\eta}$ has a typical soliton-like shape (Figure 11a), with opposing velocities in the upper/lower depth (Figure 11b). In spite of its coarse 4 m vertical resolution, the composite shear has maximum values at the
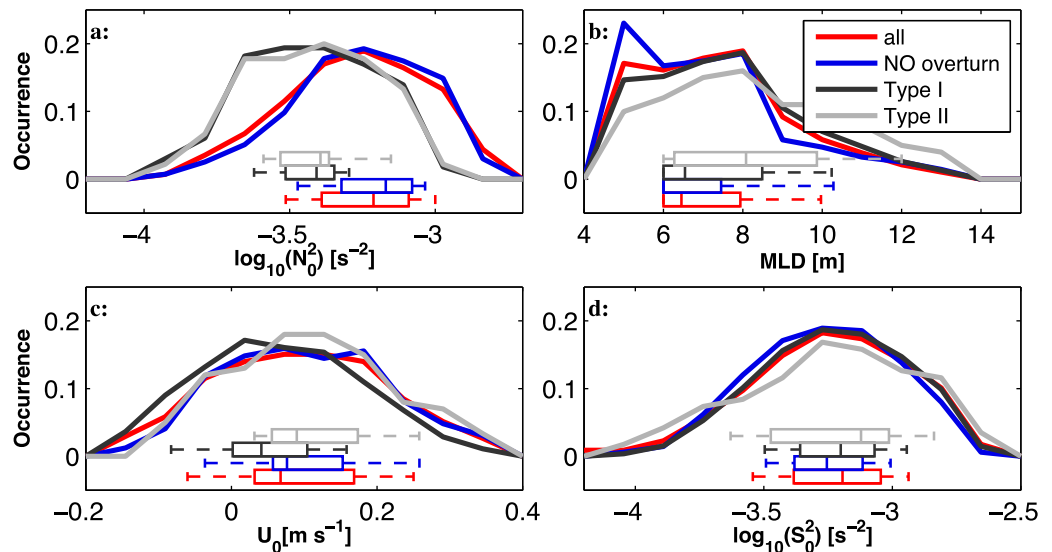

Figure 10. Same as in Figure 9, but for background parameters, including (a) near-surface stratification $\log_{10}(N_0^2)$, (b) mixed-layer depth, (c) background flow U_0, and (d) shear $\log_{10}(S_0^2)$.
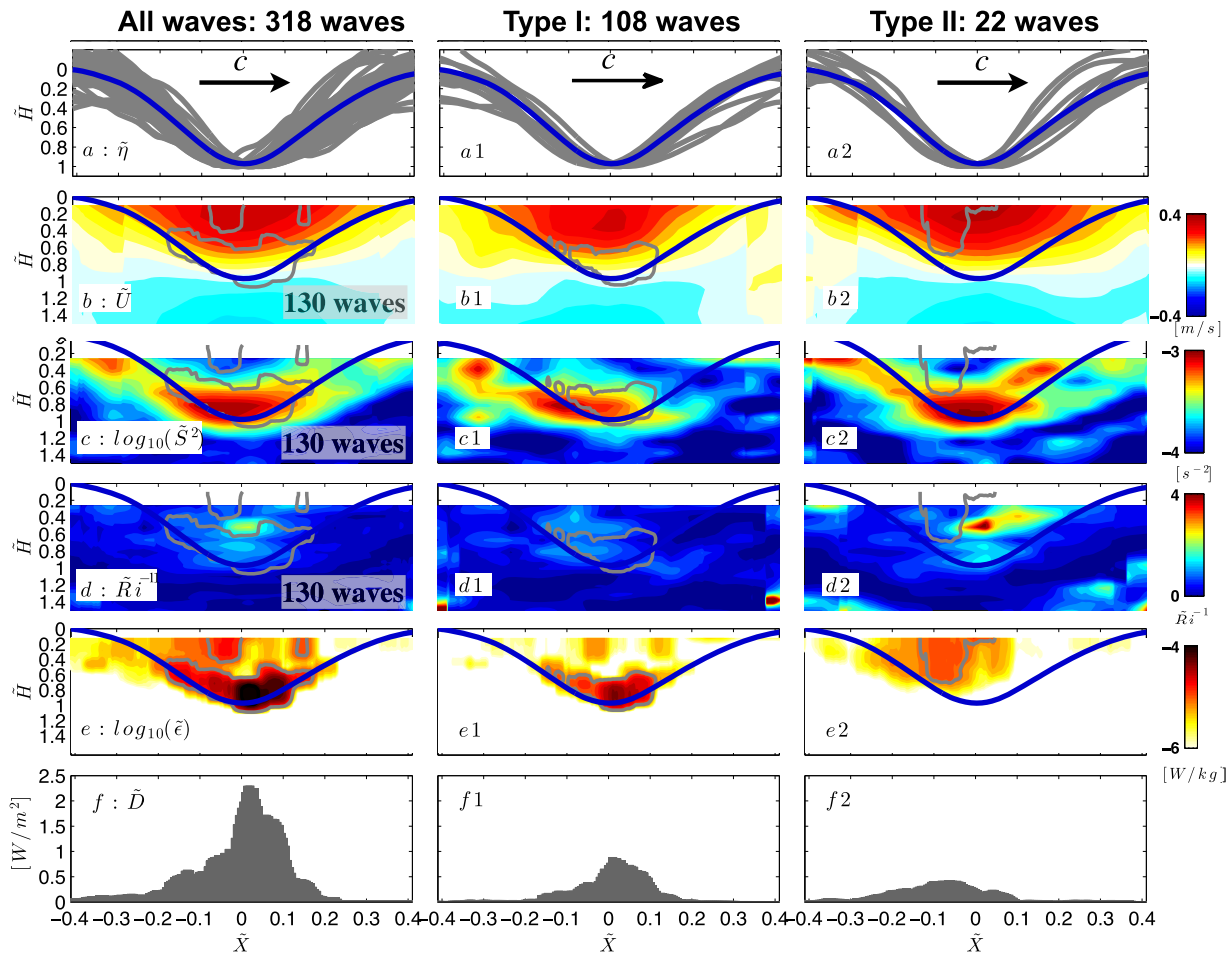
Figure 11. (left column) Composites for all waves with overturns, (middle column) Type I, and (right column) Type II waves in a normalized wave coordinate system (see text), showing (a, a1, and a2) wave maximum isotherm displacements (gray) and their composite (blue); (b, b1, and b2) composite velocity; (c, c1, and c2) composite 4 m vertical shear; (d, d1, and d2) inverse Richardson number; (e, e1, and e2) composite dissipation rate; and (f, f1, and f2) depth-integrated dissipation. Gray lines in second to fifth rows indicate 10^{-5} W kg^{-1}. A number of 130 waves are used for composites in Figures 11b, 11c and 11d due to early failure of ADCP.

wave interface (Figure 11c), roughly colocated with low Richardson numbers (Figure 11d). Note that due to the early failure of the ADCP, only a subset of 130 waves is included in the composites for Figures 11b–11d. The highest values of $\tilde{\epsilon}$ (Figure 11e) and $\tilde{D}$ (Figure 11f) occur at the wave trough and extend toward the trailing edge, as observed by *Moum et al.* [2003]. They suggested that compressed streamlines ahead of the wave trough generate a thin layer of accelerated fluid with high strain and initiate shear instability at the wave trough, which in turn generates a trailing edge and turbulent wake after the trough (their Figure 22). The existence of this pattern in many-wave composites confirms the general importance of the mechanism. Dissipation rate is also elevated throughout the wave core (Figure 11f, gray contours), indicating the influence of Type II waves.

5.2. Composites Within Each Wave Category

The composites over all waves show high dissipation at the interface (expected for Type I) and in the wave core (expected for Type II). We form composites for each wave type ($Fr < 1$ and $Fr > 1$, respectively) to attempt to distinguish the structure of the two instability mechanisms.

For the Type I wave state (108 waves: $Fr < 1$, Figure 11, middle column), composite shear is concentrated along the wave interface (Figure 11c1), roughly aligned with enhanced composite dissipation rate (Figure 11c1, gray contours). The composite inverse Richardson number is maximum in the same region, but smaller than the critical value (Figure 11d1), similar to observations in *Moum et al.* [2003], likely owing to the insufficient sampling resolution (4 m) of velocity. The composite dissipation rate $\tilde{\epsilon}$ is maximum in the

region of high values of shear (Figure 11e1), with the highest dissipation rates at the wave trough and extending toward the trailing edge (Figure 11f1). Depth-integrated dissipation value peaks at $1\,W\,m^{-2}$ around the wave trough (Figure 11f1) but is higher at the trailing edge than the leading edge, consistent with *Moum et al.* [2003].

For the Type II wave state (22 waves: $Fr > 1$, Figure 11, right column), composite dissipation rate has a very different pattern from Type I, showing a maximum inside the wave core (Figure 11e2), where composite velocity is largest (Figure 11b2) and shear is low (Figure 11c2), as expected for waves with convective instabilities, when water speed is faster than the wave propagation speed. Note that the average $\tilde{U}$ within Type II waves is much larger ($0.28\,m\,s^{-1}$) than the Type I wave ($0.1\,m\,s^{-1}$) because of the $Fr > 1$ criterion. Depth-integrated dissipation has a small peak at $0.5\,W\,m^{-2}$, but is fairly evenly distributed throughout the core and the trailing edge (Figure 11f2).

Comparing the composite quantities for Type I, Type II, and all the waves (Figure 11), $\tilde{\epsilon}$ in Type I waves suggests stronger, highly focused dissipation in contrast to that in Type II, which is weaker and widely spread over the wave core, and not as large as those observed in the first category. This is consistent with observations in *Shroyer et al.* [2010], who observe that most waves with high dissipation rates are shear driven with turbulence focused in the trailing edge. Note that the composite dissipation of all waves (Figures 11e and 11f) is greater than that of either Type I or II (Figures 11e1, 11f1, 11e2, and 11f2), because the categorized composites only include data from earlier in the season when waves are weaker.

6. Summary and Discussion

We have documented observed instabilities in NLIWs on the Washington (WA) continental shelf based on a 6 month record from a highly resolved thermistor chain/ADCP mooring. Overturning instabilities >2 m were detected in 318 waves out of a total 657 waves and their Thorpe scale-inferred turbulence documented. For the 130 wave subset for which velocity measurements were obtained, composite averages in wave coordinates were used to demonstrate that the spatial structure of the waves' dissipation could be associated with two mechanisms: shear instability (Type I) and convective instability (Type II). Using a Froude number (Fr) criterion, 108 of these 130 waves are identified as Type I ($Fr < 1$) waves and 22 as Type II ($Fr > 1$). Enhanced dissipation rates occur at the sheared interface trailing the wave trough for Type I waves, while Type II waves have elevated dissipation throughout the wave core, as found by *Moum et al.* [2003] and *Shroyer et al.* [2010] based on a much smaller sample. Overall, Type I waves are more common, and usually provide more mixing per wave, suggesting that shear instability is the more important of the two mechanisms at our location.

A significant result of our work is the lack of a clear correlation between the instability mechanism and either wave properties (e.g., amplitude, steepness, direction or energy; Figure 9) or background parameters (e.g., background stratification, mixed-layer depth and background flow; Figure 10). (Exceptions are that overturning waves tend to (1) be marginally larger and steeper and (2) occur when prewave stratification is weaker.) This poor correspondence parallels the previous finding of *Zhang et al.* [2015] that wave characteristics such as shape, amplitude, and energy likewise had no relationship to background fields apart from internal tide energy which presumably fuels them. While in some ways this near-complete lack of predictive skill is surprising, it is understandable given the known sensitivity of (1) NLIW formation to background conditions [e.g., *Helfrich and Melville*, 1986; *Stepanyants*, 2006; *Venayagamoorthy and Fringer*, 2012], (2) their propagation to the strength, direction and shear of background currents along their path [e.g., *Stastna and Lamb*, 2002; *Moum et al.*, 2007a], and (3) the anticipated sensitivity of instability to a variety of factors [e.g., *Moum et al.*, 2008]. Specifically, a number of previous laboratory and numerical studies [e.g., *Helfrich*, 1992; *Lamb*, 2002; *Fringer and Street*, 2003; *Boegman et al.*, 2005; *Aghsaee et al.*, 2010] have discussed breaking mechanisms of NLIWs, concluding that they are affected by (i) wave steepness, (ii) bottom slope, and (iii) background oceanographic conditions (e.g., pycnocline thickness, near-surface stratification, background flow/shear). These dependences are likely nonlinear and therefore difficult to demonstrate in observational data, particularly at only one site. Our lack of information at the generation site and along the propagation path are likely particularly limiting in this regard.

The continental shelf/slope region is a complex environment for NLIWs and many other process (e.g., winds, tides, and buoyancy forcing). These processes, together or independently, generate mixing that is known to be important to coastal ecosystems. This study suggests that intermittent, highly variable mixing due to

NLIWs is an important player, and supports the dominance of the shear instability and convective instability mechanisms (particularly the former) in giving rise to it. The long-term or time-integrated effects of NLIW-induced mixing, the relative importance of their breaking mechanisms, and their relative importance to other processes in coastal regions are still poorly known and require further investigation, ideally with coordinated three-dimensional models and observations.

References

Aghsaee, P., L. Boegman, and K. G. Lamb (2010), Breaking of shoaling internal solitary waves, *J. Fluid Mech.*, *659*, 289–317.

Alford, M., and R. Pinkel (2000), Patterns of turbulent and double diffusive phenomena: Observations from a rapid profiling conductivity probe, *J. Phys. Oceanogr.*, *30*, 833–854.

Alford, M. H., and R. Pinkel (2000), Observations of overturning in the thermocline: The context of ocean mixing, *J. Phys. Oceanogr.*, *30*, 805–832.

Alford, M. H., M. C. Gregg, and M. A. Merrifield (2006), Structure, propagation and mixing of energetic baroclinic tides in Mamala Bay, Oahu, Hawaii, *J. Phys. Oceanogr.*, *36*(6), 997–1018.

Boegman, L., G. N. Ivey, and J. Imberger (2005), The degeneration of internal waves in lakes with sloping topography, *Limnol. Oceanogr. Methods*, *50*(5), 1620–1637.

D'Asaro, E., R. Lien, and F. Henyey (2007), High-frequency internal waves on the Oregon continental shelf, *J. Phys. Oceanogr.*, *37*(7), 1956–1967.

Dillon, T. M. (1982), Vertical overturns: A comparison of Thorpe and Ozmidov length scales, *J. Geophys. Res.*, *87*, 9601–9613.

Duda, T. F., and D. M. Farmer (1999), *The 1998 WHOI/IOS/ONR internal solitary wave workshop: Contributed papers*, technical report No. WHOI-99-07, DTIC Document, Woods Hole Oceanogr. Inst., Mass.

Fringer, O. B., and R. L. Street (2003), The dynamics of breaking progressive interfacial waves, *J. Fluid Mech.*, *494*(494), 319–353.

Gill, A. E. (1982), *Atmosphere-Ocean Dynamics*, vol. 30, 662 pp., Academic Press.

Helfrich, K. R. (1992), Internal solitary wave breaking and run-up on a uniform slope, *J. Fluid Mech.*, *243*, 133–154.

Helfrich, K. R., and W. Melville (1986), On long nonlinear internal waves over slope-shelf topography, *J. Fluid Mech.*, *167*(1), 285–308.

Howard, L. N. (1961), Note on a paper of John W. Miles, *J. Fluid Mech.*, *10*, 509–512.

Lamb, K. (2002), A numerical investigation of solitary internal waves with trapped cores formed via shoaling, *J. Fluid Mech.*, *451*, 109–144.

Lamb, K. G. (2014), Internal wave breaking and dissipation mechanisms on the continental slope/shelf, *Annu. Rev. Fluid Mech.*, *46*, 231–254.

Levine, M. D., and T. J. Boyd (2006), Tidally forced internal waves and overturns observed on a slope: Results from HOME, *J. Phys. Oceanogr.*, *36*(6), 1184–1201.

MacKinnon, J. A., and M. C. Gregg (2003), Mixing on the late-summer New England Shelf-Solibores, shear, and stratification, *J. Phys. Oceanogr.*, *33*, 1476–1492.

MacKinnon, J. A., and M. C. Gregg (2005), Spring mixing: Turbulence and internal waves during restratification on the New England Shelf, *J. Phys. Oceanogr.*, *35*(12), 2425–2443.

Mater, B. D., S. M. Schaad, and S. K. Venayagamoorthy (2013), Relevance of the Thorpe length scale in stably stratified turbulence, *Phys. Fluids*, *25*, 076604.

Miles, J. W. (1961), On the stability of heterogeneous shear flows, *J. Fluid Mech.*, *10*, 496–508.

Moum, J. N., and J. Nash (2009), Mixing measurements on an equatorial ocean mooring, *J. Atmos. Oceanic Technol.*, *26*, 317–336.

Moum, J. N., D. M. Farmer, W. D. Smyth, L. Armi, and S. Vagle (2003), Structure and generation of turbulence at interfaces strained by internal solitary waves propagating shoreward over the continental shelf, *J. Phys. Oceanogr.*, *33*, 2093–2292.

Moum, J. N., D. Farmer, E. Shroyer, W. Smyth, and L. Armi (2007a), Dissipative losses in nonlinear internal waves propagating across the continental shelf, *J. Phys. Oceanogr.*, *37*(7), 1989–1995.

Moum, J. N., J. M. Klymak, J. D. Nash, A. Perlin, and W. D. Smyth (2007b), Energy transport by nonlinear internal waves, *J. Phys. Oceanogr.*, *37*, 1968–1988.

Moum, J. N., J. Nash, and J. Klymak (2008), Small-scale processes in the coastal ocean, *Oceanography*, *21*(4), 22–33.

Sandstrom, H., and J. A. Elliott (1984), Internal tide and solitons on the Scotian shelf: A nutrient pump at work, *J. Geophys. Res.*, *89*, 6415–6426, doi:10.1029/JC089iC04p06415.

Sandstrom, H., and N. S. Oakey (1995), Dissipation in internal tides and solitary waves, *J. Phys. Oceanogr.*, *25*, 604–614.

Schafstall, J., M. Dengler, P. Brandt, and H. Bange (2010), Tidal-induced mixing and diapycnal nutrient fluxes in the Mauritanian upwelling region, *J. Geophys. Res.*, *115*, C10014, doi:10.1029/2009JC005940.

Sharples, J., C. M. Moore, A. E. Hickman, P. M. Holligan, J. F. Tweddle, M. R. Palmer, and J. H. Simpson (2009), Internal tidal mixing as a control on continental margin ecosystems, *Geophys. Res. Lett.*, *36*, L23603, doi:10.1029/2009GL040683.

Shroyer, E., J. Moum, and J. Nash (2010), Energy transformations and dissipation of nonlinear internal waves over New Jersey's continental shelf, *Nonlinear Processes Geophys.*, *17*, 345–360, doi:10.5194/npg-17-345-2010.

Stanton, T. P., and L. A. Ostrovsky (1998), Observations of highly nonlinear internal solitons over the continental shelf, *Geophys. Res. Lett.*, *25*, 2695–2698, doi:10.1029/98GL01772.

Stastna, M., and K. Lamb (2002), Large fully nonlinear internal solitary waves: The effect of background current, *Phys. Fluids*, *14*, 2987–2999.

Stepanyants, Y. (2006), On stationary solutions of the reduced Ostrovsky equation: Periodic waves, compaction and compound solitons, *Chaos Solitons Fractals*, *28*, 193–204.

Thorpe, S. (1977), Turbulence and mixing in a Scottish Loch., *Philos. Trans. R. Soc. London A*, *286*, 125–181.

Venayagamoorthy, S., and O. Fringer (2012), Examining breaking internal waves on a shelf slope using numerical simulations, *Oceanography*, *25*(2), 132–139.

Wang, Y. H., C. F. Dai, and Y. Y. Chen (2007), Physical and ecological processes of internal waves on an isolated reef ecosystem in the South China Sea, *Geophys. Res. Lett.*, *34*, L18609, doi:10.1029/2007GL030658.

Zhang, S., M. H. Alford, and J. B. Mickett (2015), Characteristics of nonlinear internal waves on the Washington continental shelf, *J. Geophys. Res. Oceans*, *120*, 741–758, doi:10.1002/2014JC010393.